

A NEW APPROACH TO THE INTERNAL CALIBRATION OF REVERBERATION MAPPING SPECTRA

M. M. FAUSNAUGH¹

¹Department of Astronomy, The Ohio State University, 140 W 18th Ave, Columbus, OH 43210, USA

ABSTRACT

We present a new procedure for the internal (night-to-night) calibration of time series spectra, with specific applications to optical AGN reverberation mapping data. The traditional calibration technique assumes that the narrow [OIII] λ 5007 emission line profile is constant in time; given a reference [OIII] λ 5007 line profile, nightly spectra are aligned by fitting for a wavelength shift, a flux rescaling factor, and a change in the spectroscopic resolution. We propose the following modifications to this procedure: 1) we stipulate a constant spectral resolution for the final calibrated spectra, 2) we employ a more flexible model for changes in the spectral resolution, and 3) we use a Bayesian modeling framework to assess uncertainties in the calibration. In a test case using data for MCG+08-11-011, these modifications result in a calibration precision of ~ 1 millimagnitude, which is approximately a factor of five improvement over the traditional technique. At this level, other systematic issues (e.g., the nightly sensitivity functions and FeII contamination) limit the final precision of the observed light curves. We implement this procedure as a `python` package (`mapspec`), which we make available to the community.

1. INTRODUCTION

Reverberation mapping (RM, [Blandford & McKee 1982](#); [Peterson 1993, 2014](#)) is a very successful way of exploring the spatially unresolved structures in active galactic nuclei (AGN). The conspicuous broad emission lines observed in Seyfert 1 and quasar spectra respond to continuum variations on weekly to monthly time scales. Measurements of the time delay between the continuum signal and the emission line “echoes” establish the characteristic size of the line-emitting gas. This technique has become a primary means of estimating the masses of super-massive black holes that are associated with AGN activity ([Peterson et al. 2004](#); [Bentz & Katz 2015](#)). On shorter or longer time scales (less than a few days or greater than a month), lags between the UV, optical, and IR continua provide a means of applying RM to the accretion disk or the “dusty torus” (e.g., [Kishimoto et al. 2007](#); [Shappee et al. 2014](#); [Vazquez et al. 2015](#); [Edelson et al. 2015](#); [Fausnaugh et al. 2016](#)). On even longer times scales (several years to decades), narrow emission line reverberations can probe structures up to several tens of parsecs across ([Peterson et al. 2013](#)).

Crucial to RM measurements is a precise estimate of the intrinsic variability of the AGN. Such estimates require a treatment of extrinsic sources of variability, such as those created by differences in observing conditions from night to night. Studies that fail to do this will attribute extrinsic variability to the intrinsic AGN emission. [Barth & Bentz \(2016\)](#) analyze an example of such a problem in detail. The usual approach is to model and remove these extrinsic variations by assuming that some component of the AGN spectrum is

constant over the full time series. The narrow [OIII] λ 5007 emission line serves as a practical choice, since it originates in an extended region of the AGN (tens to hundreds of light years across) and should be constant over the course of a typical RM campaign (a few months). It is also relatively uncontaminated with other spectral features, although blending with variable FeII emission and the red wing of $H\beta$ can sometimes be problematic.

The traditional implementation of the rescaling model is that of [van Groningen & Wanders \(1992, hereinafter GW92\)](#). The GW92 model uses an empirical template to correct a series of observations for differences in wavelength solution, attenuation, and spectral resolution, and routinely reaches night-to-night precisions of 3–5%. As RM data have improved (e.g., [Denney et al. 2010](#); [Grier et al. 2012](#); [Du et al. 2016](#)), it has been possible to reach precisions closer to 1–3%, and sometimes even better (0.5–0.7%, [Barth et al. 2015](#)). Over the last 25 years, only minor modifications have been applied to the original GW92 approach. For example, [Barth et al. \(2015\)](#) updated the GW92 optimization procedure from a grid-search to a down-hill simplex algorithm. Occasionally, studies bypass the rescaling procedure all together; [Kaspi et al. \(2000\)](#) and [Du et al. \(2014\)](#) corrected all extrinsic variations using simultaneous observations of comparison stars. Another approach is to forgo the empirical template and model the narrow line emission with parametric functions. This is the approach adopted by the Sloan Digital Sky Survey Reverberation Mapping project ([Shen et al. 2015, 2016](#)) using the `PrepSpec` software developed by Keith Horne. [Hu et al. \(2016\)](#) recently employed a similar modeling tech-

nique to improve the calibration of RM data taken in 2008 of MCG-6-30-15 from 2% to 0.5%.

Considering the gains in computing resources over the last two decades and the rise of alternative model-fitting techniques, we decided to investigate more substantial modifications to the GW92 procedure. In §2 we review the main elements of the GW92 rescaling model and propose three improvements. We then discuss a new model and fitting procedure to implement these modifications, and we make our implementation available to the community as a `python` package called `mapspec` (MCMC Algorithm for Parameters of Spectra).¹ In §3, we assess our method by applying it to new RM data for MCG+08-11-011 (UCG 3374) that has been presented more completely elsewhere (Fausnaugh et al. 2017). We find that the precision of the night-to-night calibration increases by roughly a factor of five using our new approach, and the final light-curve uncertainties are dominated by intrinsic systematic effects that require more complicated methods to address. In §4, we summarize these results, and we include a brief appendix that discusses the influence of correlated errors on our results.

2. THE APPROACH OF GW92 AND PROPOSED IMPROVEMENTS

The GW92 approach aligns the [OIII] $\lambda 5007$ line profile of some observed spectrum O to a reference spectrum \hat{R} by applying a wavelength shift, a flux rescaling factor, and a smoothing kernel. The shift accounts for differences in the wavelength solution, the rescaling factor for differences in attenuation (e.g., atmospheric extinction), and the smoothing kernel for differences in resolution (e.g., changes in seeing or spectrograph focus).

To fit for these parameters, GW92 use a grid search. The current model parameters are applied to O to create a rescaled spectrum \tilde{O} , and the alignment with \hat{R} is determined using the difference spectrum $\tilde{D} = \hat{R} - \tilde{O}$. Near a narrow emission line with constant flux (such as [OIII] $\lambda 5007$), the only difference between \hat{R} and \tilde{O} should be intrinsic continuum and broad-line flux variations. Therefore, \tilde{D} should be a smooth function of wavelength, and GW92 use the χ^2 of a low-order polynomial fit to \tilde{D} to measure of the alignment between \hat{R} and \tilde{O} :

$$\chi^2 = \sum_{\lambda} \frac{[\tilde{D}(\lambda) - P(\lambda)]^2}{\sigma_{\hat{R}}^2(\lambda) + \tilde{\sigma}_O^2(\lambda)} \quad (1)$$

where $P(\lambda)$ is the polynomial, $\sigma_{\hat{R}}$ is the uncertainty on \hat{R} and $\tilde{\sigma}_O$ is the uncertainty on \tilde{O} . Note the P is fit directly to \tilde{D} and that χ^2 is always minimized with respect to the polynomial; the rescaling model is considered optimized when χ^2 is minimized with respect to \tilde{D} by finding the model parameters that

best align \tilde{O} with \hat{R} .

To account for changes in resolution, the GW92 model uses a Gaussian smoothing kernel. The main effect of changing the resolution is to change the width of the observed emission lines. GW92 therefore parameterize the spectral resolution using the full width at half maximum (FWHM) of the [OIII] $\lambda 5007$ line. Seeing variations are usually small from night to night, so changes in resolution are generally small compared to the width of narrow emission lines, and practically negligible compared to the width of broad emission lines.

A complication arises because \hat{R} may have a higher resolution (lower FWHM) than O . Since deconvolution is numerically unstable, GW92 also test models where \hat{R} is smoothed to match O —if the resulting χ^2 is smaller than smoothing O to match \hat{R} , then O is inferred to have a lower resolution (higher FWHM) than \hat{R} . In these cases, the final rescaled spectrum \tilde{O} is not corrected for resolution, so as to avoid deconvolution.

This method has been very effective in past RM campaigns (e.g.,s Peterson et al. 2004; Bentz et al. 2009; Denney et al. 2010; Barth et al. 2011; Grier et al. 2012; Barth et al. 2013; Pei et al. 2014; Barth et al. 2015). However, we suggest several modifications to improve this approach.

1. **Resolution.** Because GW92 chose to ignore resolution corrections for cases where O is observed at lower resolution (greater FWHM) than \hat{R} , the final set of rescaled spectra exist at a variety of resolutions. The minimum FWHM is defined by \hat{R} , since the model will smooth O to match \hat{R} whenever possible, while the maximum FWHM is set by the epoch with the worst resolution. This means that any quantity calculated from the ensemble spectra (for example, the mean spectrum), has additional scatter from the heterogeneous resolutions. We instead construct \hat{R} so that its resolution matches the *worst* resolution (largest FWHM) of the time series. This will guarantee that the model always prefers to smooth O to match \hat{R} , and \hat{R} will therefore define a single resolution of the rescaled spectra.
2. **Smoothing Kernel.** While a Gaussian smoothing kernel is a good first-order approximation for changes in the resolution from night to night, the true kernel can be significantly more complicated. For example, there are changes due to miscentering in the slit, changing spectrograph focus, guiding errors, and flexure in the telescope/optics system. Using a smoothing kernel that is more complex than a Gaussian should lead to an improved nightly calibration, and we use Gauss-Hermite polynomials to parameterize this complexity. A similar approach is often taken when measuring the line-of-sight velocity dispersion in galaxy spectra (e.g., van der Marel & Franx 1993).

¹ <https://github.com/mmfausnaugh/mapspec>

3. **Model Uncertainties.** While minimizing χ^2 on a grid is computationally efficient, this approach can make estimating model uncertainties difficult. GW92 did not rigorously consider uncertainties in the model parameters, although they show that these uncertainties are smaller than any “by eye” rescaling approach. We instead use a Bayesian framework when optimizing the rescaling parameters, which can naturally account for model uncertainties from the parameters’ posterior probability distributions.

2.1. Reference Spectrum

The first step of the calibration is to construct a high signal-to-noise ratio (S/N) reference spectrum. The reference defines the flux scale of the calibrated time series, so the usual practice is to combine spectra from photometric nights—this ensures that the final time series corresponds to physical fluxes. We construct the reference by averaging the photometric spectra, weighting each observation at epoch t_i by the measurement uncertainty $\sigma_O(\lambda)$. The uncertainty in the reference is therefore $\sigma_R(\lambda) = (\sum_i 1/\sigma_O^2(\lambda, t_i))^{-1/2}$. Even with a moderate number of spectra, the uncertainty in any observed spectrum will be much larger than the uncertainty in the reference.

Our first modification relates to the resolution of the reference. When averaging the photometric spectra, the resulting resolution roughly corresponds to the average resolution of the input spectra (in practice, we have found this to be the case, see §3). We then smooth the reference so that its resolution matches the lowest resolution of all the observations. Like GW92, we estimate the spectral resolution with the width of the narrow [OIII] $\lambda 5007$ emission line, using the FWHM of Gaussians fit to the observed line profiles. Although the true [OIII] $\lambda 5007$ line profiles are more complex, this simple method provides a good relative comparison. The [OIII] $\lambda 5007$ FWHM in the smoothed reference then defines the final resolution of the entire time series.

2.2. Model Details and Fitting Procedure

We model the rescaled spectrum \tilde{O} from an observed spectrum O as

$$\tilde{O}(\lambda) = a \int_{-\infty}^{\infty} O(\lambda-s)K(\lambda-\lambda')d\lambda' \quad (2)$$

where a is a flux scaling factor, s is a wavelength shift, and K is a smoothing kernel. We assume that O has an accurate relative flux calibration (that the slope of the continuum is correct) and that O is free of aperture effects (that the flux from extended sources such as the host-galaxy and narrow line region is fixed; see Peterson et al. 1995). The smoothing kernel is a sum of Gauss-Hermite polynomials

$$K(\lambda-\lambda') = e^{u^2/2} \sum_{i=0}^N b_i H_i(u) \quad ; \quad u = \frac{\lambda-\lambda'}{w} \quad (3)$$

where the lowest order term $i=0$ is a simple Gaussian with width w , $H_i(u)$ are the Gauss-Hermite polynomials following the definition of van der Marel & Franx 1993, and b_i are coefficients to be optimized. We adopt

$$b_0 = 1 \quad b_1 = b_2 = 0 \quad (4)$$

and truncate the series at $N=4$, which gives the coefficients a simple interpretation: b_3 quantifies asymmetric deviations from a Gaussian, similar to skewness, and b_4 quantifies symmetric deviations, similar to kurtosis (van der Marel & Franx 1993). Since the H_i are orthogonal on the Gaussian weighting function, b_3 and b_4 are uncorrelated, simplifying the fitting procedure. Under this formalism, we can recover a simple Gaussian model by taking $N=0$, or we can add arbitrary complexity by extending the series beyond $N=4$.

We simultaneously fit for a , s , w , and any b_i using Markov Chain Monte Carlo (MCMC) methods. The MCMC searches for parameters that minimize

$$\chi^2 = \sum_{\lambda} \frac{[\hat{R}(\lambda) - \tilde{O}(\lambda)]^2}{\sigma_R^2(\lambda) + \tilde{\sigma}_O^2(\lambda)} \quad (5)$$

where $\hat{R}(\lambda)$ is the reference spectrum, $\sigma_R(\lambda)$ is its uncertainty, and $\tilde{\sigma}_O(\lambda)$ is determined by standard error propagation on the observed spectrum:

$$\tilde{\sigma}_O^2(\lambda) = a^2 \int_{-\infty}^{\infty} \sigma_O^2(\lambda-s)K^2(\lambda-\lambda')d\lambda'. \quad (6)$$

Here, $\sigma_O^2(\lambda-s)$ is the uncertainty from interpolation. Linear interpolation is usually adequate with $\sigma_O^2(\lambda_{i+1}-s) = (1-x)^2\sigma_O^2(\lambda_{i+1}) + x^2\sigma_O^2(\lambda_i)$ where x is the fractional pixel shift $s/(\lambda_{i+1}-\lambda_i)$.

Minimizing χ^2 is equivalent to maximizing the log-likelihood of the data given the model, assuming normally distributed and uncorrelated residuals. We discuss the possible influence of correlated residuals in the Appendix. Equation 5 also implicitly assumes uniform (uninformative) priors on the parameters, but alternative choices of prior parameter distributions are fully supported by the `mapspec` implementation (see below).

Only non-variable parts of \hat{R} and \tilde{O} should be compared, i.e., the narrow [OIII] $\lambda 5007$ line. We isolate the emission line by subtracting a local linear-interpolation of the underlying continuum. We remove large wavelength offsets of the spectra by cross-correlation, which finds the shift to the nearest pixel, so that the parameter s should usually be less than a pixel. When performing the fit, we ignore 5% of the data on each end of the fitting window—this avoids edge effects from the convolution and helps stabilize the number of degrees of freedom (the overlap of the spectra can change for large values of the wavelength shift s). The kernel width w is restricted to be greater than or equal to half a pixel—at smaller values, the smoothing kernel is indistinguishable from a δ -function. We also explicitly normalize K so that

$\int_{-\infty}^{\infty} K d\lambda = 1$, which conserves flux and helps prevent correlations between the rescaling factor a and parameters that define K . Finally, we restrict b_3 and b_4 to lie between -0.3 and 0.3 . Empirical experiments indicate that this range is a small enough for the MCMC chain to converge quickly, while it is large enough to produce a wide range of line profiles.

The MCMC procedure automatically produces posterior probability distributions for each parameter. Examination of the posterior distributions allows us to quickly assess the quality of the fit. For example, observations taken in bad conditions will have poorly constrained parameters because of low S/N at each pixel. Such a diagnostic is not available using the traditional GW92 grid-search.

We have developed a `python` package that implements the above model and fitting procedure, which we call `mapspec` (MCMC Algorithm for Parameters of Spectra) and make freely available. The software is object-oriented to facilitate modularity and extensibility. The package also includes data structures that naturally organize spectroscopic data and provide useful operations and analysis methods, such as interpolation, rebinning, line extraction/integration, velocity percentile calculation, etc. These data structures are well suited for use on any spectrum with emission lines. A variety of data formats are supported, including `ascii`, comma-separated value, and fits files. Template scripts are provided that help construct a reference spectrum and fit the model to a given time series. Finally, the software supports a flexible implementation of priors during the fitting procedure—the user may specify any analytic probability density function as a prior on any parameter in the model. Posteriors distributions from previous `mapspec` runs can also be imported for use as priors on future fits.

3. TEST CASE: MCG+08-11-011

We compared our new approach to that of GW92 using the time series spectra of MCG+08-11-011 (UGC 3774) from a recent RM campaign (Fausnaugh et al. 2017). Data were taken on the 1.3m McGraw-Hill telescope at the MDM observatory in Spring of 2014. MCG+08-11-011 is a low-redshift source ($z \approx 0.02$, $V \approx 14.8$ magnitude) that exhibited strong and coherent variability during the RM campaign.

3.1. Reference Spectrum

We constructed the reference from 18 spectra taken on six photometric nights as reported by the observers. We checked the photometric list of observations by calculating the [OIII] $\lambda 5007$ line flux in each spectrum. We subtracted a local linearly-interpolated continuum underneath the line and integrated the remaining flux using Simpson’s method. We then applied iterative 3σ clipping to the array of line flux measurements, which removed three spectra from the photometric list. Our final estimate of the [OIII] $\lambda 5007$ line flux is $(6.13 \pm 0.02) \times 10^{-13}$ erg cm $^{-2}$ s $^{-1}$, calculated from the remaining 15 spectra.

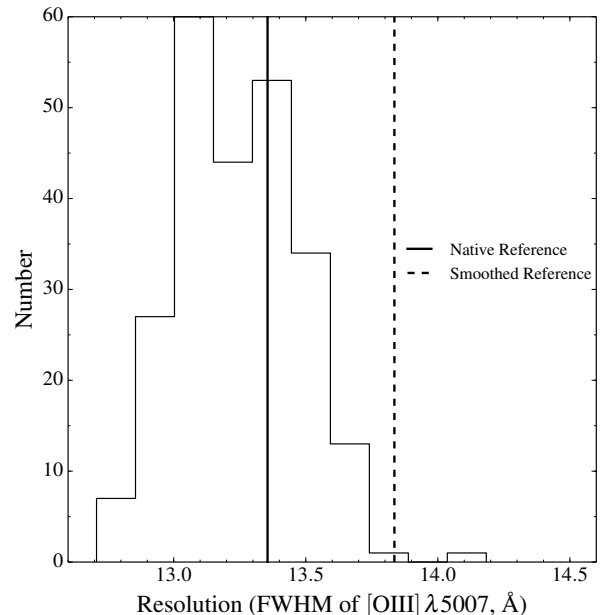


Figure 1. Distribution of spectral resolutions for the full time series, estimated by the FWHM of Gaussians fit to the narrow [OIII] $\lambda 5007$ line profiles. The resolution of the reference spectrum constructed from photometric nights is shown with the solid line, the resolution of the reference after smoothing is shown with the dashed line.

We combined these spectra with a noise-weighted average to make an initial estimate of the reference spectrum at its “native” resolution. During this step, we used MCMC methods to fit for the wavelength shift that best aligns the [OIII] $\lambda 5007$ profiles of the spectra in a least-squares sense. The reference sets the final wavelength grid, so it is important to adopt a single and consistent wavelength solution when averaging. However, the absolute accuracy of this solution does not matter for the purpose of the night-to-night calibration (in practice, we chose a wavelength solution accurate to 0.5 Å, as measured by night-sky lines).

We estimated the resolutions of the input spectra with the FWHM of Gaussians fitted to [OIII] $\lambda 5007$ line profiles. The mean FWHM of these spectra is 13.35 Å, very close to the value measured in the weighted average spectrum of 13.36 Å.² Next we created a smoothed reference whose resolution matches the lowest resolution spectrum of the full time series. The distribution of [OIII] $\lambda 5007$ FWHM mea-

² A more rigorous estimate of the spectral resolution is obtained by subtracting in quadrature the intrinsic line width from the observed line width. Whittle (1992) gives the intrinsic FWHM of the [OIII] $\lambda 5007$ line in MCG+08-11-011 as 605 km s $^{-1}$. This corresponds to 10.52 Å in the observed frame and gives a spectral resolution of 8.22 Å. However, the only effect of this correction is to shift the distribution in Figure 1 by a constant amount, so we omit this correction here. Note that Whittle (1992) measure the FWHM directly from the line profile instead of using a Gaussian fit. If we measure the FWHM in the “native” reference in the same way, we find a value of 12.63 Å. This implies a spectral resolution of 6.99 Å, the value adopted by Fausnaugh et al. in preparation.

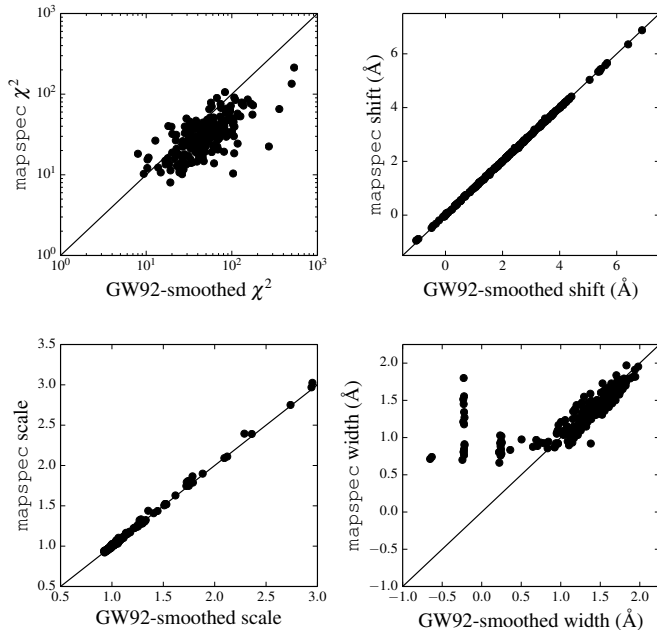


Figure 2. Comparison of parameters fit by the GW92 algorithm and the `mapspec` procedure. The solid lines show one-to-one relations. A negative width indicates that the GW92 method prefers to smooth the reference to match the observation, and the output spectra are not smoothed in these cases.

measurements from the full time series is shown in Figure 1. The FWHM measurement above 14.0 \AA appears to be an outlier that could be explained by especially bad seeing or large guiding errors that caused the target to move in the slit. We therefore took the next-largest FWHM of the distribution (13.75 \AA) as the worst resolution of the time series. We smoothed the “native” reference with a Gaussian kernel of FWHM = 3.26 \AA to produce a smoothed reference with a resolution of FWHM = 13.84 \AA . This will set the final resolution of the rescaled time series.

3.2. Comparison of `mapspec` and GW92

We compared the `mapspec` fits to two different implementations of the GW92 method. The first implementation rescales the time series to match the “native” reference and allows a heterogeneous set of output resolutions, as per the original GW92 approach. The second method aligns the time series to the smoothed reference with the same GW92 model. This allows us to independently compare the effects of adopting a single resolution for the final spectra with the effects of the `mapspec` model and fitting procedure. We designate the first approach the GW92 method and the second approach the GW92-smoothed method.

In Figure 2, we compare the parameters found by `mapspec` to those of the GW92 scaling procedure (for the smoothed reference only, since we do not expect the kernel widths to match for different reference spectra). There is excellent agreement between the two models, especially for

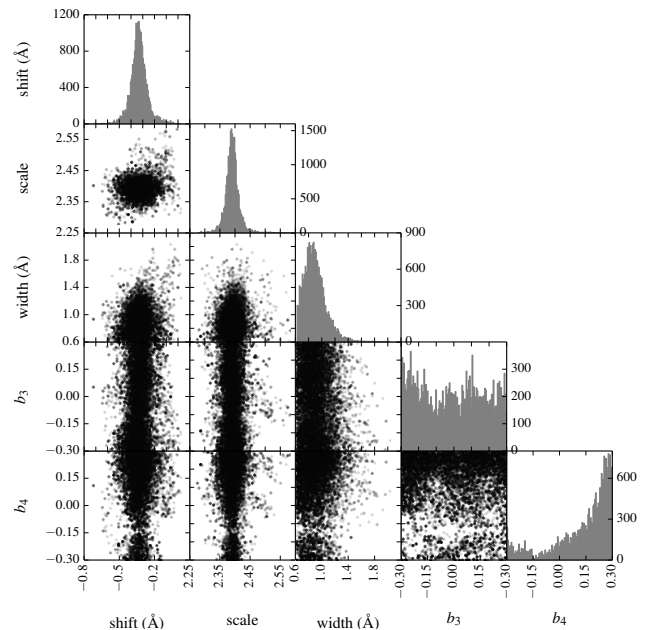


Figure 3. Example of posterior parameter distributions for the observation on 2014 April 17 UT. The conditions were partly cloudy with persistent thick cirrus, and the spectrum requires significant rescaling. The model prefers a peakier line profile, but the skewness is unconstrained (the best fit value of b_3 is 0.0).

the shift and rescaling parameters. The dispersion is somewhat larger for the width parameter, but our models are not identical and we do not expect a perfect match. Negative widths for the GW92 procedure indicate spectra with FWHM greater than that of the reference, and are not smoothed when rescaling. In principle, the algorithm should always prefer to smooth the observation to match the reference; the cases with negative FWHM might be due to the grid-search algorithm, which can converge to a local rather than global minimum, or to limitations in the smoothing model itself (a pure Gaussian). The values of χ^2 for both fits also track each other reasonably well, although they are not defined in the same way (see Equations 1 and 5). The `mapspec` model tends to have smaller χ^2 values than the GW92 procedure, which may be a result of the additional `mapspec` parameters.

In terms of performance, it takes 8352 seconds of user-time (2.3 hours) to calibrate 240 observations of MCG+08-11-011 (on average, three observations every night for 80 nights). For comparison, the GW92 grid-search requires 75 seconds to run on the same data. Although `mapspec` takes over 100 times longer to run than the GW92 algorithm, it provides the additional benefits of a more general and flexible model, and saves the posterior probability distributions of the parameters. Since each spectrum is considered independently, the amount of user time can be greatly reduced simply by distributing the calibration processes across several computers.

In Figure 3, we show a set of posterior distributions for one spectrum taken on 2014 April 17 UT. Conditions were

partly cloudy with persistent cirrus clouds, and the observation required significant rescaling. The best-fit parameters are $a = 2.38$, $s = -0.34 \text{ \AA}$, $w = 0.92 \text{ \AA}$, $b_3 = 0.00$, and $b_4 = 0.29$. The wavelength shift s and flux rescaling factor a are very well constrained, with the sizes of the central 68% confidence intervals equal to 0.01 \AA and 1% of the of the median rescaling factor, respectively. The posterior distribution of the kernel width w is somewhat broader, and while there is no constraint on the skewness, the model clearly prefers a peaky line profile.

In general, we find that the wavelength shift and flux rescaling parameters are similarly well-constrained for all observations, while the kernel shapes show a wide combination of widths, skewness, and kurtosis. In one case (2014 January 29 UT), we found that the scaling parameter was poorly constrained (the central 68% interval of the posterior distribution was 6% of the median value). Visual inspection of this spectrum showed an anomalous “shelf” on the blue wing of the [OIII] $\lambda 5007$ line that is not present in any other spectrum. For this night, weather conditions consisted of patchy clouds, and the anomalous feature may be due to movement of the target in the slit if the guide star was temporarily lost during the observation. We therefore exclude this observation from the final data set. This procedure demonstrates the diagnostic utility of carefully examining the posterior probability distributions.

One caveat is that there is very little FeII emission in MCG+08-11-011, and the [OIII] $\lambda 5007$ line is not blended with $H\beta$. In other AGN, the [OIII] $\lambda 5007$ line is strongly blended with these variable components and it is not easy to isolate the narrow line flux with a local linearly-interpolated continuum. We have tested our method on objects farther along the Eigenvector 1 sequence (Boroson & Green 1992) with weak [OIII] $\lambda 5007$ and very strong FeII emission, and we found that neither `mapspec` nor the GW92 approach provided a reasonable calibration. The `mapspec` procedure may still be useful for such spectra, but a more sophisticated means of separating the narrow line from the continuum, FeII, and possibly $H\beta$ emission would be required.

3.3. Mean and RMS Spectra

We compare the output spectra from different rescaling procedures using the mean and root-mean-square (rms) residual spectra of the time series. The mean spectrum $\bar{F}(\lambda)$ is the average of the rescaled spectra, weighted by the measurement uncertainties after propagation through the model. The rms spectrum is

$$F_{\text{rms}}(\lambda) = \sqrt{\frac{1}{N-1} \sum_i^N [\tilde{O}(\lambda, t_i) - \bar{F}(\lambda)]^2}. \quad (7)$$

Figure 4 shows the mean and rms spectra from the GW92, GW92-smoothed, and `mapspec` methods. The mean spectra are almost indistinguishable—the only visible difference is a

peakier [OIII] $\lambda 5007$ in the original GW92 method, which is expected because the reference was not smoothed for this procedure. The rms spectra are also very similar—the continuum and broad lines are virtually indistinguishable between the three methods.

There are noticeable differences in the rms spectrum near the [OIII] $\lambda 4959$ and [OIII] $\lambda 5007$ line profiles, which are highlighted in the insets in Figure 4. We see large residuals across both narrow line profiles for the GW92 method. The GW92-smoothed method has similar but smaller residuals, mainly confined to the wings of the lines. This shows that a substantial fraction of the rms residuals are due to the heterogeneous resolution of the original GW92 approach. These [OIII] residuals vanish when using the `mapspec` model, presumably due to the more flexible line profiles afforded by the Gauss-Hermite polynomials. Close inspection of the $H\beta$ line-profile also shows that the narrow component has been more cleanly removed from the rms spectrum by the `mapspec` approach.

Suppression of the [OIII] and $H\beta$ narrow line residuals is an important benefit of the `mapspec` approach. The rms spectrum isolates the variable part of the spectrum, so the velocity of the reverberating gas is usually measured from the line-width of the rms line-profile. The presence of spurious variability, such as residuals from narrow line profiles, can affect these line-width measurements. This effect is not very important in these data, since the broad $H\beta$ line has essentially no overlap with the [OIII] lines, and the differences between the GW92 and `mapspec` $H\beta$ rms profiles are small. However, in other AGN the red wing of $H\beta$ is often blended with the [OIII] lines, and/or the narrow $H\beta$ component is more significant compared to the broad component (see, e.g., Grier et al. 2012 and Fausnaugh et al. 2017, for several examples). For such objects, suppressing systematic errors in the nightly calibration represents a more substantial improvement in the reliability of line-width measurements.

Finally, suppressing the [OIII] residuals may provide a means of identifying FeII variability. The FeII multiplet lines at 4924 \AA and 5018 \AA are blended with the narrow [OIII] lines, and these features are impossible to measure underneath the large [OIII] residuals caused by the GW92 approach. Using `mapspec`, the smoothness of the continuum at these wavelengths suggests that it may be possible to detect FeII variability for other objects. However, we know that very strong FeII emission will cause the calibration to fail (§3.2), so more testing is required to assess `mapspec`’s potential in this regard.

3.4. Light Curves

The final goal of the night-to-night calibration is to measure intrinsic flux variations, i.e., light curves. In Figure 5, we show three light curves extracted from the time series spectra—the continuum at 5100 \AA (rest-frame), the integrated broad $H\beta$ line, and the integrated [OIII] $\lambda 5007$ line.

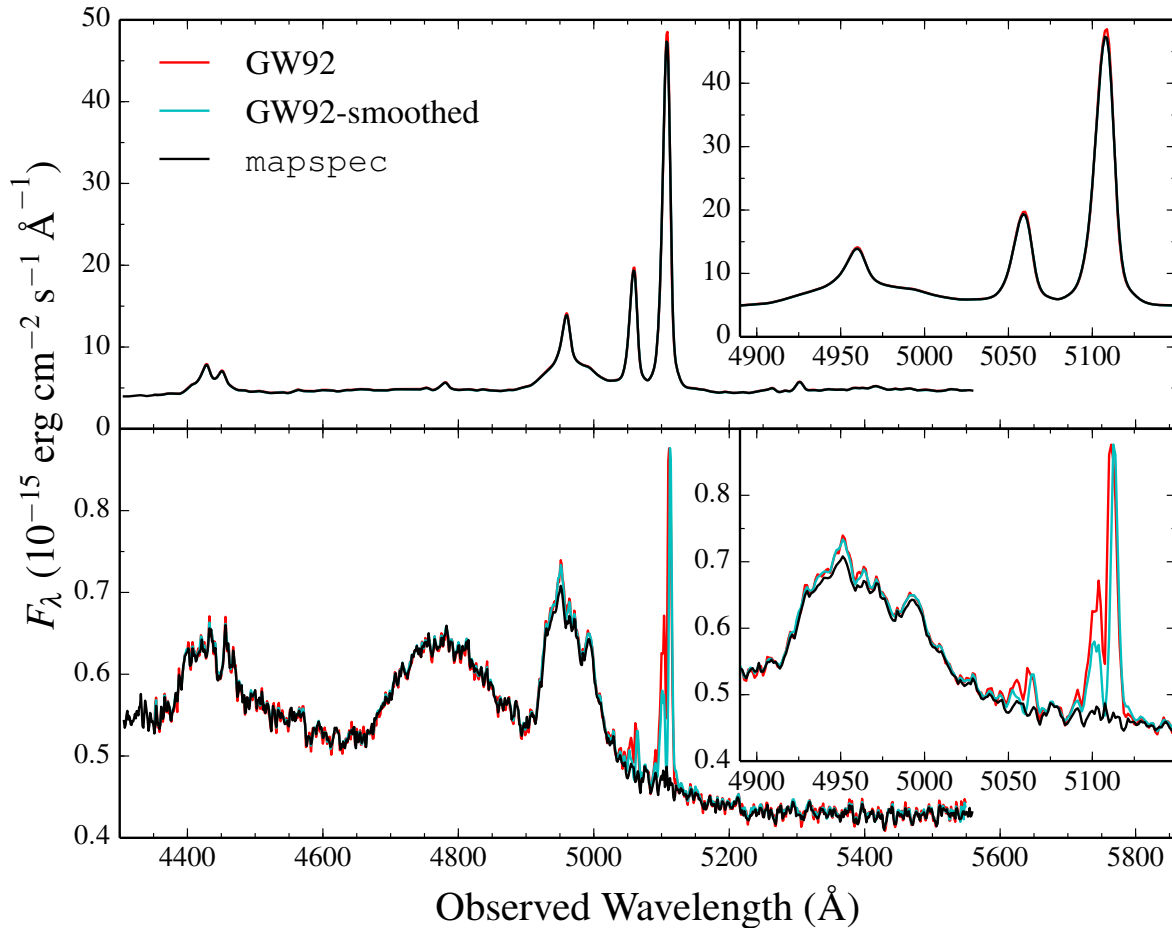


Figure 4. Comparison of the mean and rms spectra derived from the three rescaling methods. GW92 is the original [van Groningen & Wanders \(1992\)](#) method, using a reference constructed from photometric nights and left at its native resolution. GW92-smoothed uses the same procedure but with a smoothed reference (see §2.1). `mapspec` is the result from the model described in §2.2. Note the dramatic suppression of the [OIII] residuals in the `mapspec` approach.

The continuum light curve was estimated using the average flux density over the observed wavelength region between 5190 and 5230 Å, and its uncertainty is the sample standard deviation in this window. The H β line flux was estimated by subtracting a local linear approximation of the underlying continuum and integrating the remaining flux using Simpson’s method. We did not correct for the narrow H β component, which contributes a constant flux-offset to these measurements. Line flux uncertainties were estimated using a Monte Carlo approach: the spectrum was perturbed 10^3 times by random Gaussian deviates scaled to the flux uncertainty at each wavelength (including correlations introduced by smoothing, see the Appendix), and the line was re-extracted and integrated for each iteration. We adopt the width of the central 68% confidence interval of the resulting distribution as an estimate of the line-flux uncertainty. An identical procedure was applied to the [OIII] $\lambda 5007$ line.

It is clear that the choice of calibration procedure makes

only a small difference for the continuum and H β light curves. This result might be expected based on the similarity of the mean and rms spectra at these wavelengths (Figure 4). However, the `mapspec` approach greatly reduces the scatter in the [OIII] $\lambda 5007$ line light curve compared to the GW92 method. Following [Barth et al. \(2013\)](#), the scatter in the [OIII] $\lambda 5007$ light curve serves as an estimate of the remaining uncertainty in the night-to-night calibrations. The fractional scatter in the `mapspec` [OIII] $\lambda 5007$ light curve is 0.09% (or zero if adjusted for the line-flux uncertainties, see [Barth et al. 2013, 2015](#)). This is roughly a factor of five gain over the 0.52% scatter of the original GW92 approach. For other data sets, precisions of 3% to 5% are sometimes the best attainable with the GW92 approach, in which case a factor of five improvement is much more meaningful. From the same 2014 campaign, we also have data for 3C 382 and Mrk 374. The GW92 approach resulted in calibrations precise to 1.83% for 3C 382 and 1.95% for Mrk 374, measured

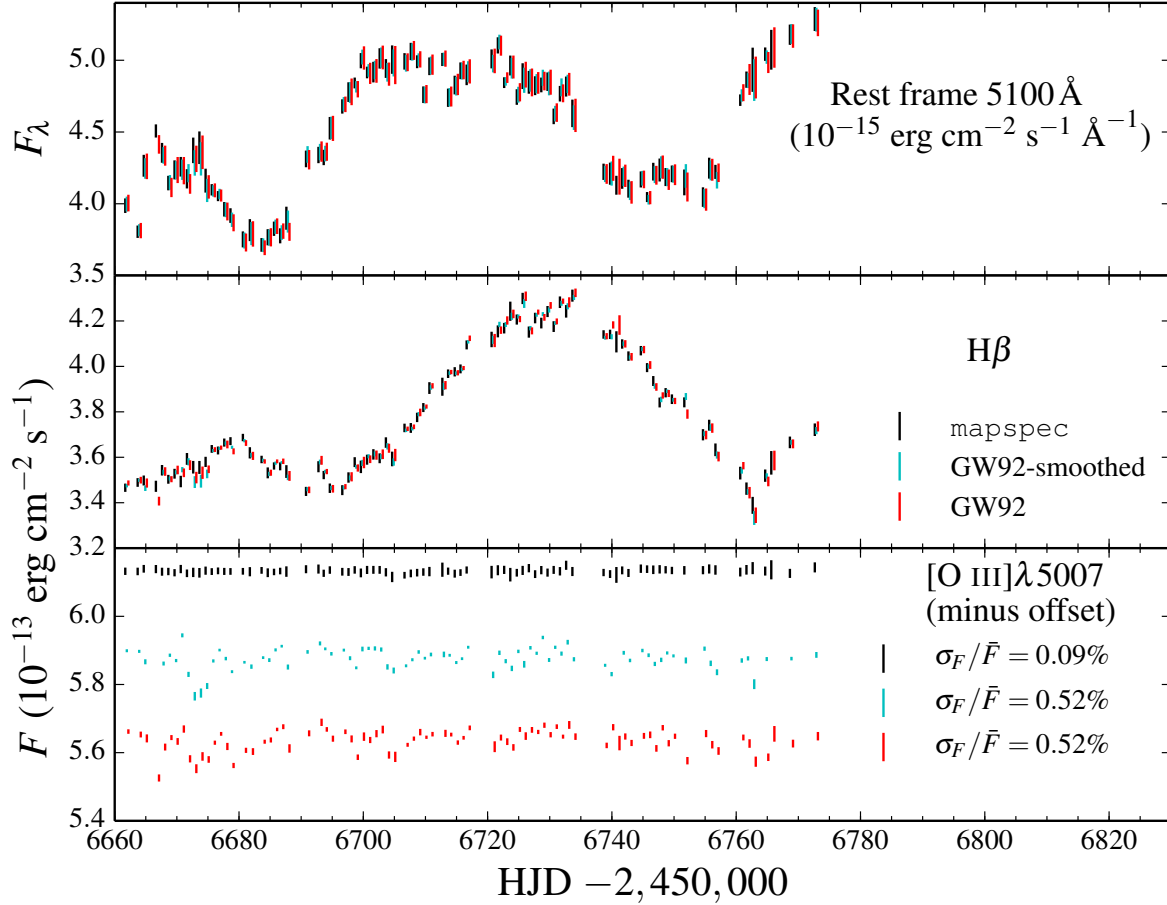


Figure 5. Comparison of light curves extracted from spectra calibrated with the three different procedures. GW92, GW92-smoothed, and `mapspec` correspond to the same methods as in Figure 4. For clarity, the data from different rescaling methods have been given a small offset along the abscissas, as well as along the ordinates for the [OIII] $\lambda 5007$ light curves. The choice of rescaling method changes the amount of scatter in the [OIII] $\lambda 5007$ line light curve by a factor of five, quantified by the fractional root-mean-square scatter σ_F/\bar{F} .

using the [OIII] $\lambda 5007$ light curves in the same way as for MCG+08-11-011. These are more typical results, and the `mapspec` approach improves the calibrations to 0.92% for 3C 382 (a factor of 2) and 0.62% for Mrk 374 (a factor of 3).

While it is not obvious from Figure 5, the differences between the `mapspec` and GW92 $H\beta$ and continuum light curves are largely due to the GW92 calibration errors. In Figure 6, we show the light curve differences (the red points minus the black points in Figure 5) as a function of [OIII] $\lambda 5007$ flux from both procedures. Since the `mapspec` [OIII] $\lambda 5007$ light curve is virtually flat, we see no correlation of the $H\beta$ and continuum light curve differences with the `mapspec` [OIII] $\lambda 5007$ fluxes. However, the light curve differences are strongly correlated with the GW92 [OIII] $\lambda 5007$ fluxes, illustrating how the GW92 calibration errors add noise to the resulting $H\beta$ and continuum light curves.

The `mapspec` calibration precision is nominally $\sim 0.1\%$ (millimagitudes). However, there are other systematic effects

that limit the final precision of the light curves:

- Errors in the relative flux calibrations of the spectra will affect the observations regardless of any rescaling model. The relative flux calibration depends on the nightly sensitivity functions, which are themselves calculated from observations of standard stars. The night-to-night repeatability of the sensitivity functions therefore depends on the choice of standard star, the observing conditions, and even the choice of image reduction and fitting techniques. It is likely that this uncertainty enters at the 1% level or higher. Errors in the relative flux calibration will result in biased flux measurements for large wavelength windows or for wavelength windows farther from the [OIII] $\lambda 5007$ emission line.
- Uncertainties in the continuum subtraction will affect the integrated line flux. Although our Monte Carlo approach accounts for part of this uncertainty, there

are additional errors introduced by the choice of the wavelength windows used to define the continuum. The continuum may also be more complicated than the simple linear model employed here.

- Variable spectral components besides the continuum and broad-line emission will affect the light curve measurements. For example, FeII contamination, which is a problem at all optical wavelengths, can add additional variability as it reverberates out of phase with both the continuum and the emission lines (Barth et al. 2013). Variable amounts of host-galaxy light also enter the spectral extraction aperture due to variations in seeing, which will appear as noise in the final light curves (Peterson et al. 1995).

Methods besides the rescaling method presented here are necessary to account for these systematic errors. Spectral decomposition can help address the issue of variable spectral components, although such a decomposition will introduce its own set of uncertainties (i.e., model-dependent flux estimates). Relative flux calibration, on the other hand, requires great effort and extreme care to reduce below 1%—even in a recent RM campaign using COS on board of *HST* (for which the sensitivity function is very well known), the uncertainty floor for repeatability was roughly 1.1% (De Rosa et al. 2015).

4. SUMMARY

We have developed a new procedure for night-to-night calibration of time-series spectra. The main innovations of our method are 1) a common and consistently defined resolution, 2) a more flexible smoothing kernel, and 3) a Bayesian formalism for fitting the line profiles and estimating parameter uncertainties. We have shown that the method improves the alignment of the [OIII] line profiles, decreasing spurious variability in the rms spectrum and integrated [OIII] λ 5007 line light curve. These improvements help isolate the variable broad emission-line profiles and reduce night-to-night calibration uncertainties. Other systematic effects limit the final precision of the light curves, such as the calculation of nightly sensitivity functions and contamination from additional spectral components such as FeII emission.

MMF thanks Richard Pogge for the suggestion to improve the GW92 method, Chris Kochanek for useful discussions about statistics, and Brad Peterson for general guidance. MMF also thanks Kelly Denney, Gisella de Rosa, Catherine Grier, Kevin Croxall, Richard Pogge, and Brad Peterson for tips on reducing and analyzing spectroscopic data. MMF acknowledges financial support from NSF grant AST-1008882 and a Presidential Fellowship awarded by The Ohio State University Graduate School.

Facility: McGraw-Hill

Software: Astropy (Astropy Collaboration et al. 2013),

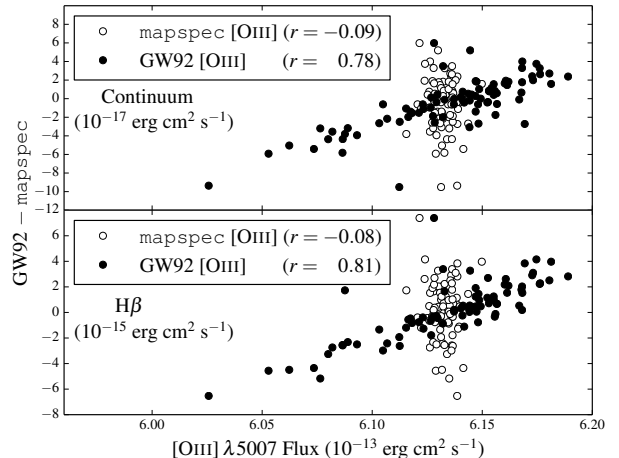


Figure 6. Differences between the continuum and $H\beta$ light curves from different calibration procedures (red points minus black points in Figure 5) as a function of [OIII] λ 5007 line flux. [OIII] λ 5007 line fluxes from the GW92 procedure are shown with solid points, [OIII] λ 5007 line fluxes from *mapspec* are shown with open points. The Pearson r correlation coefficients are shown in the legends. These correlations show that errors in the GW92 [OIII] λ 5007 calibration introduce noise in the continuum and line light curves.

Matplotlib (Hunter 2007), Numpy (van der Walt et al. 2011), Scipy (Oliphant 2007)

APPENDIX—COVARIANCES INTRODUCED BY THE MODEL

The rescaling model presented here introduces correlations in the data because of interpolation and smoothing. These correlations can affect integrated quantities, for example, the χ^2 used to fit the model parameters and the uncertainties in the integrated line flux. In this appendix, we assess the importance of these correlations.

The covariance matrix for a vector $\tilde{\mathbf{y}}$ derived from a vector \mathbf{y} is

$$\text{cov}(\tilde{y}_m, \tilde{y}_n) = \sum_i \sum_j \frac{\partial \tilde{y}_m}{\partial y_i} \frac{\partial \tilde{y}_n}{\partial y_j} \text{cov}(y_i, y_j) \quad (8)$$

(Gardner 2003). If $\tilde{\mathbf{y}}$ is derived from linear interpolation on \mathbf{y} , covariances are introduced between adjacent points. Similarly, smoothing introduces local covariances that depend on the width of the kernel. The covariances from smoothing are probably larger than those from interpolation—for simplicity, we only discuss smoothing in what follows, although the *mapspec* implementation includes both.

In practice, the convolution in Equation 2 must be implemented as a discrete sum:

$$\tilde{O}(\lambda_m) = \sum_i O(\lambda_i) K(\lambda_i - \lambda_m) \quad (9)$$

$$\tilde{O}_m = \sum_i O_i K_m \quad (10)$$

so the covariance is

$$\text{cov}(\tilde{O}_m, \tilde{O}_n) = \sum_i \sum_j K_m K_n \text{cov}(O_i, O_j). \quad (11)$$

Assuming that the original data are uncorrelated, then $\text{cov}(O_i, O_j)$ is diagonal and

$$\text{cov}(\tilde{O}_m, \tilde{O}_n) = \sum_i K_m K_n \sigma_i^2, \quad (12)$$

which reduces to Equation 6 if we ignore off-diagonal terms. The error spectrum $\sigma_O(\lambda_i) = \sigma_i$ is estimated during the data reduction/spectral extraction. It consists of the photon-counting noise and read noise on each pixel. In general, the data in adjacent pixels *are* expected to be correlated, but the covariance matrix is not known *a priori*. It may be possible to estimate/model this covariance, perhaps using Gaussian processes in a manner similar to Garnett et al. (2017), but such an analysis is beyond the scope of this work. We assume that the original data are uncorrelated here.

In Figure 7, we show the covariance matrix for wavelengths near the [OIII] lines in the rescaled spectrum from a photometric night (2014 January 10 UT). There is clearly a strong local covariance structure, which is most visible near the emission lines. An investigation of the impact of these correlations on the χ^2 of the `mapspec` fits and the integrated line flux uncertainty is therefore warranted.

If we define $\mathcal{C} = \text{cov}(\tilde{O}_m, \tilde{O}_n)$, we can rewrite Equation 5 for a general χ^2

$$\chi^2 = \mathbf{D}^T \mathcal{C}^{-1} \mathbf{D} \quad (13)$$

where $\mathbf{D} = \hat{R}(\lambda) - \tilde{O}(\lambda)$ is the column vector of residuals. In principle, \hat{R} has some associated covariance matrix \mathcal{R} , so we should replace \mathcal{C}^{-1} with $(\mathcal{C} + \mathcal{R})^{-1}$. We have experimented with including this covariance, and found that it makes virtually no difference to the fits.

We found that including the full covariance matrix \mathcal{C} reduces the χ^2 by noticeable amounts, but does not change the best fit parameters of the rescaling model. This is not surprising—we can already tell from the good alignment of the [OIII] $\lambda 5007$ line profiles that the fits are nearly optimized (Figure 4). Including the covariance structure also does not affect the posterior distributions of the model parameters, although there is some tendency for the MCMC chains to burn-in faster. However, this gain does not compensate for the extra time required to repeatedly calculate and invert \mathcal{C} during the MCMC, so we revert to Equation 5 when performing the fits.

To quantify the effect of correlations on the uncertainty of the integrated line flux, we used H β as a test case and employed two methods. First, we integrated the line profile using a Monte Carlo method: for 10^3 iterations, we extracted the line flux after adjusting the spectrum by random Gaussian deviates scaled to the measurement uncertainties propagated through the rescaling model. Second, we repeated this pro-

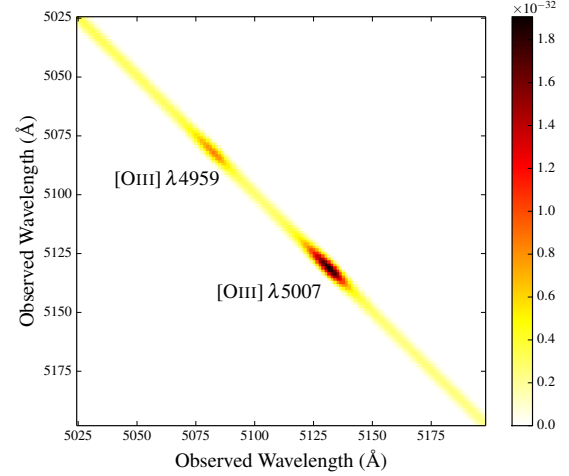


Figure 7. Example covariance matrix for wavelengths near the [OIII] emission lines, calculated for an observation from 2014 January 10 UT after applying the rescaling model. The color bar shows the covariance in squared physical units, $(\text{erg s}^{-1} \text{cm}^{-2} \text{Å}^{-1})^2$. There are significant local correlations, which can affect integrated quantities such as the χ^2 used to fit the rescaling model.

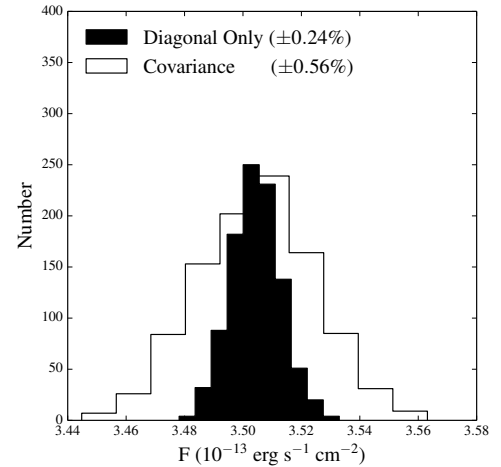


Figure 8. Distribution of broad H β line fluxes using the Monte Carlo methods described in the Appendix. The widths (central 68% intervals) of the distributions serve as an estimate of the integrated line flux uncertainty. Ignoring correlations in the line profile results in underestimated uncertainties by a factor of two.

cedure but drew deviates from the multivariate normal distribution defined by the propagated covariance matrix. The first method is equivalent to the second method if we ignore off-diagonal terms in the covariance matrix.

Figure 8 shows the distribution of integrated line fluxes for each procedure, again using the observation from 2014 January 10 UT. The presence of correlated errors is extremely important for the integrated line flux—the width of the distribution using the covariances is a factor of two larger than that using the diagonal only. This result can be intuitively understood through the integration operation itself—correlated

perturbations will tend to increase/decrease adjacent flux measurements, which magnifies the change in area under the

line profile. We therefore include the correlations when calculating the line flux uncertainties in §3.5.

REFERENCES

- Astropy Collaboration, Robitaille, T. P., Tollerud, E. J., et al. 2013, *A&A*, 558, A33
- Barth, A. J., & Bentz, M. C. 2016, *MNRAS*, 458, L109
- Barth, A. J., Pancoast, A., Thorman, S. J., et al. 2011, *ApJ*, 743, L4
- Barth, A. J., Pancoast, A., Bennert, V. N., et al. 2013, *ApJ*, 769, 128
- Barth, A. J., Bennert, V. N., Canalizo, G., et al. 2015, *ApJS*, 217, 26
- Bentz, M. C., & Katz, S. 2015, *PASP*, 127, 67
- Bentz, M. C., Walsh, J. L., Barth, A. J., et al. 2009, *ApJ*, 705, 199
- Blandford, R. D., & McKee, C. F. 1982, *ApJ*, 255, 419
- Boroson, T. A., & Green, R. F. 1992, *ApJS*, 80, 109
- De Rosa, G., Peterson, B. M., Ely, J., et al. 2015, *ApJ*, 806, 128
- Denney, K. D., Peterson, B. M., Pogge, R. W., et al. 2010, *ApJ*, 721, 715
- Du, P., Hu, C., Lu, K.-X., et al. 2014, *ApJ*, 782, 45
- Du, P., Lu, K.-X., Hu, C., et al. 2016, *ApJ*, 820, 27
- Edelson, R., Gelbord, J. M., Horne, K., et al. 2015, *ApJ*, 806, 129
- Fausnaugh, M. M., Denney, K. D., Barth, A. J., et al. 2016, *ApJ*, 821, 56
- Fausnaugh, M. M., Grier, C. J., Bentz, M. C., et al. 2017, *ApJ*, 840, 97
- Gardner, J. L. 2003, *Journal of Research of NIST*, 108, 69
- Garnett, R., Ho, S., Bird, S., & Schneider, J. 2017, *MNRAS*, 472, 1850
- Grier, C. J., Peterson, B. M., Pogge, R. W., et al. 2012, *ApJ*, 755, 60
- Hu, C., Wang, J.-M., Ho, L. C., et al. 2016, *ApJ*, 832, 197
- Hunter, J. D. 2007, *Computing in Science & Engineering*, 9, 90
- Kaspi, S., Smith, P. S., Netzer, H., et al. 2000, *ApJ*, 533, 631
- Kishimoto, M., Hönig, S. F., Beckert, T., & Weigelt, G. 2007, *A&A*, 476, 713
- Oliphant, T. E. 2007, *Computing in Science & Engineering*, 9, 10
- Pei, L., Barth, A. J., Aldering, G. S., et al. 2014, *ApJ*, 795, 38
- Peterson, B. M. 1993, *PASP*, 105, 247
- . 2014, *Space Sci. Rev.*, 183, 253
- Peterson, B. M., Pogge, R. W., Wanders, I., Smith, S. M., & Romanishin, W. 1995, *PASP*, 107, 579
- Peterson, B. M., Ferrarese, L., Gilbert, K. M., et al. 2004, *ApJ*, 613, 682
- Peterson, B. M., Denney, K. D., De Rosa, G., et al. 2013, *ApJ*, 779, 109
- Shappee, B. J., Prieto, J. L., Grupe, D., et al. 2014, *ApJ*, 788, 48
- Shen, Y., Brandt, W. N., Dawson, K. S., et al. 2015, *ApJS*, 216, 4
- Shen, Y., Horne, K., Grier, C. J., et al. 2016, *ApJ*, 818, 30
- van der Marel, R. P., & Franx, M. 1993, *ApJ*, 407, 525
- van der Walt, S., Colbert, S. C., & Varoquaux, G. 2011, *Computing in Science & Engineering*, 13, 22
- van Groningen, E., & Wanders, I. 1992, *PASP*, 104, 700 (GW92)
- Vazquez, B., Galianni, P., Richmond, M., et al. 2015, *ApJ*, 801, 127
- Whittle, M. 1992, *ApJS*, 79, 49